SUPPLEMENTARY MATERIALS AND METHODS

Image reconstruction

The description of the measurements in eye imaginal discs and of eye sizes in adult flies have been previously published in (Vollmer et al., 2016) and is repeated here for the convenience of the reader.

To measure the eye discs in 3D, we first reconstructed the 3D apical surface of the developing eye disc. To this end, the apical membrane was manually segmented using the aPKC-antibody staining. Neighbouring membranes (the apposing peripodial epithelium), as well as parts belonging to the antenna were removed manually. Surface reconstruction and measurements of 3D areas were done using the commercial software package Amira. To measure the geometrical properties in 2D, maximum intensity projections were done as implemented in ImageJ (Abràmoff et al., 2004), and the areas as well as the posterior length (Fig. 1B,C, yellow line) were measured using the software ImageJ. The eye disc bends in 3D such that ventral "flaps" emerge below the 2D projection of the eye disc. We measured these separately and included these in the 2D measurements. 2D measurements were extrapolated to 3D given the linear correlation of those measures (Fig. S1).

Eye sizes of adult flies were measured using ImageJ. The heads of adult flies were mounted on Hoyer's:Lactic acid (1:1) mounting medium and cleared by overnight heating. Images were taken focusing on the front and back planes of the eye to account for all eye area. Front and back areas were summed up to give the total eye area.

The shape σ, given by the ratio of major to minor axis of an ellipse was determined, by fitting an ellipse to each eye disc such that the deviation between the measured anterior (A) and posterior (P) area and the ones predicted by an ellipse with the given posterior length L_p and total area T was minimized.

Computational analysis

The eye disc growth model has been described in detail before and the following description has been adapted from (Vollmer et al., 2016) for the convenience of the reader.

Eye disc growth mainly occurs on the anterior side of the MF at rate $k(L_P)A$, where $k(L_P)$ is the area growth rate, A the anterior area, and the posterior length L_p serves as a measure of developmental time (Vollmer et al., 2016), as previous measurements established a linear relationship (Wartlick et al., 2014). Additionally, the area may change at rate $L_{MF}(L_P) \cdot (\phi - 1)$ as anterior area is converted into posterior area as a result of the MF movement. Here, L_{MF} is the length of the morphogenetic furrow (MF) in dorsal-ventral direction. The total area increase can then be described by:

$$\frac{dT}{dL_P} = k(L_P)A + L_{MF}(L_P) \cdot (\phi - 1) \quad (5)$$

We previously showed that the second term has only a minor effect (Vollmer et al., 2016). Accordingly, we used Φ=1 in all cases and thus assumed that differentiation does not alter the area. Please see (Vollmer et al., 2016) for a more detailed discussion on this. Moreover, we have

$$\frac{dP}{dL_P} = L_{MF}(L_P), \quad (6)$$

because the MF speed is $\frac{dL_P}{dL_P} = 1$ in our simulation framework. The measured MF speed, v_{MF}, can be used to convert the posterior length to real developmental time, as done for the simulations of the grafting experiments (Fig. 4C; v_{MF}= 3.4 µm/h as described in Vollmer et al., 2016). The anterior area follows as

$A = T - P$.

Since the shape of the eye disc can be approximated by an ellipse (Vollmer et al., 2016), we can use the equations for an ellipse,

$$A = T\left[1 - \frac{1}{\pi}\left(\cos^{-1}\left(1 - \frac{2L_P}{L_{AP}}\right) - 2\left(1 - \frac{2L_P}{L_{AP}}\right)\sqrt{\frac{L_P}{L_{AP}}\left(1 - \frac{L_P}{L_{AP}}\right)}\right)\right] \quad (7)$$

to calculate the current shape of the eye disc given the current values for T, A, and L_p. Here L_{AP} is the total length of the disc in anterior-posterior direction. The minor axis of length a then follows as $a = L_{AP}/2$, and the major axis of length b as $b = T/\pi a$. $L_{MF}(L_P)$ can then be determined accordingly.

Eqs. (5-7) can be simulated with any growth law $k(L_P)$, including for growth control based on pure dilution as given by Eq. 2

$$k(L_P) = k_0 \frac{T(0)}{T(L_P)},$$

or a dilution model with added degradation as given by Eq. 4

$$k(L_P) = k_0 \frac{T(0)}{T(L_P)} e^{-\delta(L_P - L_P(0))}.$$

We start the simulations with an initial posterior length L_{p0}=15μm. All other parameters for the models were optimized such that the deviation of the model from the measured area distributions for T, P and A (Fig. 1C,D) was minimized. A trust-region-reflective algorithm (Coleman and Li, 1996) was used as implemented in the lsqnonlin function in the commercial software Matlab R2016a. For ODE integration we used a forward Euler scheme.

Simulation of Transplant Experiments

Eye disc growth is substantially slower when eye discs are transplanted to the abdomen of adult flies, but similar final disc sizes are obtained (Garcia-Bellido, 1965). Given the longer developmental times, we checked whether a dilution model could still reproduce the observed growth kinetics with the needed Upd half-life of 24 hours (Fig. 2). In the reported experiments, 24 hours AEL, the 4 most anterior segments of larvae were transplanted without the brain to the abdomen of 4-day old virgin (squares, dashed line) or fertilized flies (circle, dashed line), or with brain to fertilized flies (triangles, solid line) (Garcia-Bellido, 1965). In the more slowly growing eye discs, the MF must move at a slower speed; we need to reduce v_{MF} to 5% of the value used in *GMR*>+. The maximal growth rate, k_0, needs to be reduced only to 28% of the value used for *GMR*>+. If the half-life is assumed to be 48 hours, v_{MF} needs to be reduced to 5% and k_0 to 18%. Relative values are given with respect to Table S1.

Fluorescence recovery after photobleaching

The experimental procedure for FRAP measurements has been described before and the following part has been adapted from (Fried et al., 2016) for the convenience of the reader.

Imaginal discs were dissected in SF-900 medium at room temperature (21°C), and transferred to a medium-containing well with a glass coverslip bottom. The samples were maintained at 21°C. The data analysis was done using different software applications. For the imaging analysis ImageJ v.1.47f was used; the statistics was done using the Microcal Origin v.8.1 software.

To determine the Upd diffusion coefficient, eye imaginal discs from GMR-GAL4; UAS-GFP:Upd were used (Tsai and Sun, 2004). The ROI (solid circle with a radius of 5.7 µm in Fig. 3A) was photobleached for 46 s using an Argon laser 488 nm with laser power 36.8% and transmission 100%. The recovery was observed by exciting GFP in the sample with an Argon laser 488 nm with laser power 2% and transmission 100%, pinhole 1.4 Airy units. The laser was installed on a confocal microscope Nikon Ti with 60x(1.40) VC OIL DIC objective using a camera Nikon A1, zoom 2.5x, gain ~1200. The movies have a duration of 10 min with one frame every 4 seconds, each frame with a 2-line average.

The number of samples taken to perform this analysis was n = 9. The image analysis was performed following the description in (Kang et al., 2012). Here the diffusion coefficient is defined as:

$$D = \frac{r_e^2 + r_n^2}{8 \cdot \tau_{1/2}}$$

where r_n is the nominal radius (ROI radius), r_e is the effective radius (spreading radius of postbleached profile) and $\tau_{1/2}$ is the half time of the recovery. In order to calculate r_e, the bleaching profile (Fig. 3F) can be approximate by an Gaussian profile fitting it to the following expression:

$$f(x) = 1 - K \cdot \exp\left(\frac{-x^2}{r_e^2}\right)$$

K and r_e can be obtain using a nonlinear least-squares fitting routing (nlinfit.m) available in MATLAB.

These parameters can also be obtained by applying a direct protocol. First, K can be determined from the bleaching depth in the normalized postbleach profile as referred to in Fig. 3B. Then, the half width of cross-sections between the horizontal line at the height of $0.86K$ from the bottom of the postbleach profile (Fig. 3B) and the postbleach profiles yields r_e without involving any fitting (Fig. 3B).

To measure $\tau_{1/2}$ from the FRAP data a linear interpolation method was used. $F:\{F(0),F(t_1),F(t_2),\cdots,F(t_n)\}$ such that $F(0)=F0$ and $F(t_n)=F^{\infty}$. The fluorescence intensity at half of recovery is defined as $F_{1/2}=\left(F0+F^{\infty}\right)/2$. If $F(t_k)=F_{1/2}$ for some t_k then the half-recovery time follows as $\tau_{1/2}=t_k$. If $F(t_k)<F_{1/2}<F(t_{k+1})$ it is defined as:

$$\tau_{1/2} = t_k + \frac{F_{1/2}-F(t_k)}{F(t_{k+1})-F(t_k)}(t_{k+1}-t_k)$$

Figure 3A shows one of the eye discs where the photobleaching was done. Figures 3B-E show some photobleaching recovery frames with details. A bleaching profile sample can be observed in figure 3F and the bleaching recovery profile is shown in figure 3G. According to the analysis the half recovery time is of $\tau_{1/2}$ = 1.3 min and the diffusion coefficient was calculated as D_{Upd} = 0.67 ± 0.19 μm^2 s^{-1}.

Notes on protocol:

We used an ectopically expressed GFP-tagged form of Upd to determine the diffusion coefficient and diffusion length of Upd, which allows us to infer the half-life of the Upd protein. We used Fluorescence Recovery After Photobleaching (FRAP) rather than Fluorescence Correlation Spectroscopy (FCS) to determine the diffusion coefficient, because in this way we obtain the effective diffusion coefficient over a wider distance rather than the local diffusion coefficient. Measurements by FRAP require the expression of a fluorescently-tagged protein, and all previous FRAP-based measurements of diffusion coefficient of morphogens in Drosophila imaginal discs have been carried out by overexpressing the fluorescently-tagged protein of interest (Kicheva et al., 2007). We acknowledge that saturation effects due to ligand overexpression may increase the diffusion coefficient compared to the wildtype situation such that the wildtype diffusion coefficient would be smaller. However, in case of a larger diffusion coefficient, also the diffusion length would be increased (which we establish with the same construct). As we are only interested in the degradation rate/half-life, the two effects will cancel.

Overexpression of a protein can, in principle, lead to either the generation of an abnormal form with altered half-life, or to the accumulation of a receptor-unbound form that could be more stable. However, overexpression of Upd has been shown to be active, and its molecular structure is therefore presumably preserved (Bach et al., 2003). Second, the genetic system that we use (GAL4/UAS) does not lead to saturating levels of Upd. Thus, GAL4/UAS is temperature sensitive, and the experiments for the determination of the molecular properties of Upd were carried out at 25ºC. In the range of temperatures that we use (18-29 ºC), increasing temperature (i.e. Upd production) also increases the severity of the phenotype, indicating that at 25ºC the receptor and its signaling pathway is not saturated (Fig. S8). Finally, we have now extended our previously published computational model of eye disc patterning (Fried et al., 2016) to study the effect of constitutive Upd production behind the

MF (Gmr>Upd) (Fig. S5). If we assume that the ectopic production rate of Upd per unit area is the same as the endogenous one in the posterior rim before the MF starts, then the model predicts that in the Gmr>Upd genotype, the maximal Upd concentration never exceeds the maximal Upd concentration in the control strain – so that receptor saturation will not be a problem. The reason for this observation is that a substantial ectopic production of Upd only starts with a delay when the MF has sufficiently advanced to create a sizeable posterior area. By that time, the endogenous Upd concentration has, however, already strongly declined as a result of dilution. In conclusion, saturation should not be a problem, and we expect the GFP-tagged ectopically expressed Upd to have a similar half-life as the endogenous Upd.

Supplementary Tables

Supplementary Table S1: Parameter values for *Gmr>+*, all models with $L_P(0)$ = 15 µm.

Model	$k(L_P)$	T(0) [µm^2]	k_0 [µm^{-1}]	σ(0)	δ [µm^{-1}]
P_A	$k(L_P) = k_0 \frac{T(0)}{T(L_P)}$	1.4794E+04	0.0812	5.7206	-
P_A, 6h	$k(L_P) = k_0 \frac{T(0)}{T(L_P)} e^{-\delta(L_P - L_P(0))}$	1.0844e+04	0.1903	5.6566	0.0158
P_A, 12h	$k(L_P) = k_0 \frac{T(0)}{T(L_P)} e^{-\delta(L_P - L_P(0))}$	1.2233e+04	0.1335	5.8116	0.0079
P_A, 24h	$k(L_P) = k_0 \frac{T(0)}{T(L_P)} e^{-\delta(L_P - L_P(0))}$	1.3321e+04	0.1064	5.8121	0.0040
P_A, 36h	$k(L_P) = k_0 \frac{T(0)}{T(L_P)} e^{-\delta(L_P - L_P(0))}$	1.3764e+04	0.0978	5.7934	0.0026
P_A, 48h	$k(L_P) = k_0 \frac{T(0)}{T(L_P)} e^{-\delta(L_P - L_P(0))}$	1.4003e+04	0.0935	5.7798	0.0020
P_A, 72h	$k(L_P) = k_0 \frac{T(0)}{T(L_P)} e^{-\delta(L_P - L_P(0))}$	1.4254e+04	0.0894	5.7633	0.0013
P_A, 96h	$k(L_P) = k_0 \frac{T(0)}{T(L_P)} e^{-\delta(L_P - L_P(0))}$	1.4384e+04	0.0873	5.7538	9.89e-04
EXP	$k_0 e^{-\delta(L_P - L_P(0))}$	1.5595E+04	0.0555	5.5309	0.0168

Supplementary Figures

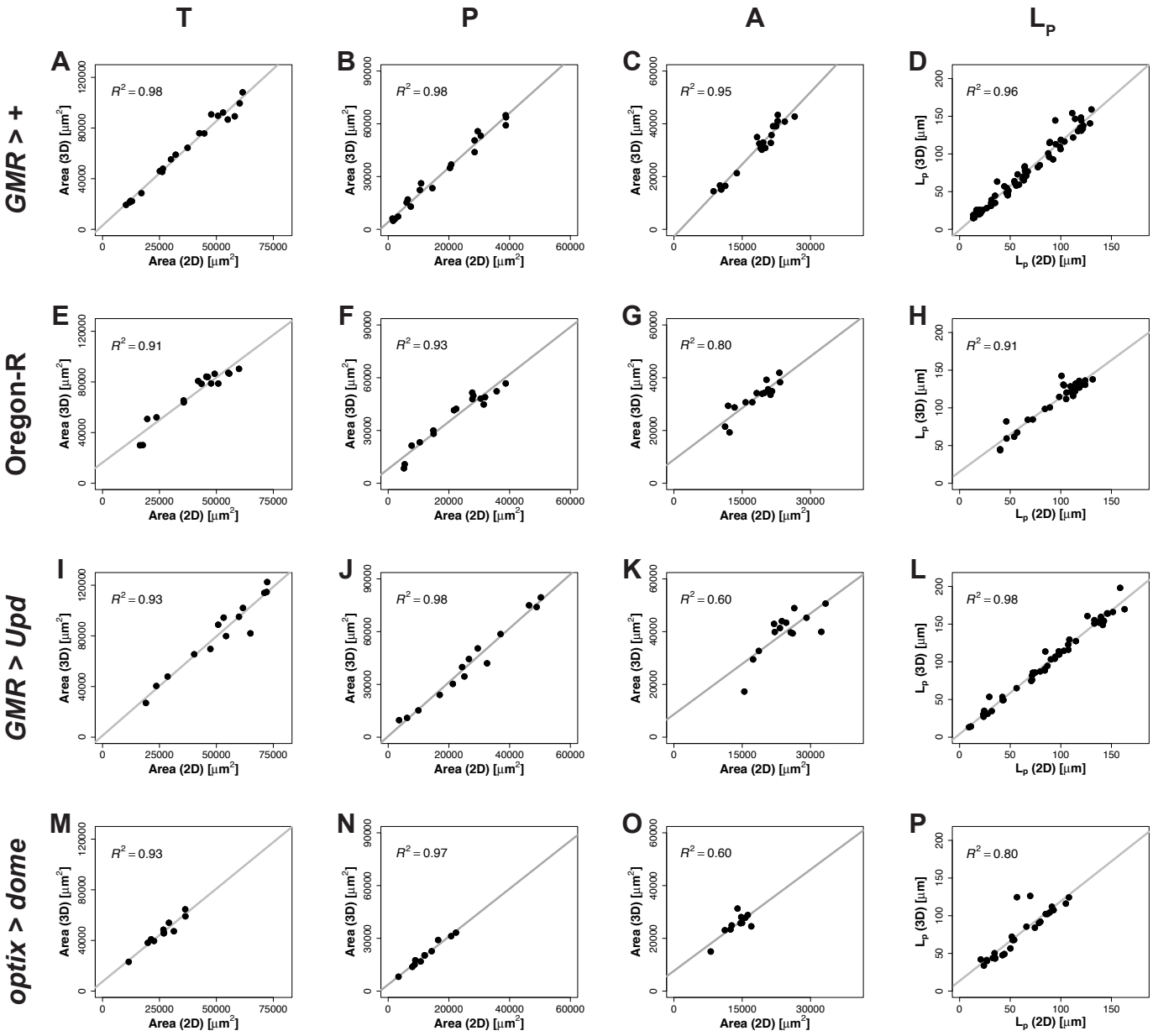

Figure S1: Correlations of 2D and 3D measurements

Linear correlation for the 2D and 3D measurements of total area (first column, A,E,I,M), posterior area (second column, B,F,J,N), anterior area (third column, C,G,K,O) and posterior length L_P (last column, D,H,L,P).

(A-D) Data for *GMR>+*. This data was taken from (Vollmer et al., 2016).

(E-H) Data for Oregon-R. This data was taken from (Vollmer et al., 2016).

(I-L) Data for *GMR>Upd*

(M-P) Data for *optix>dome*

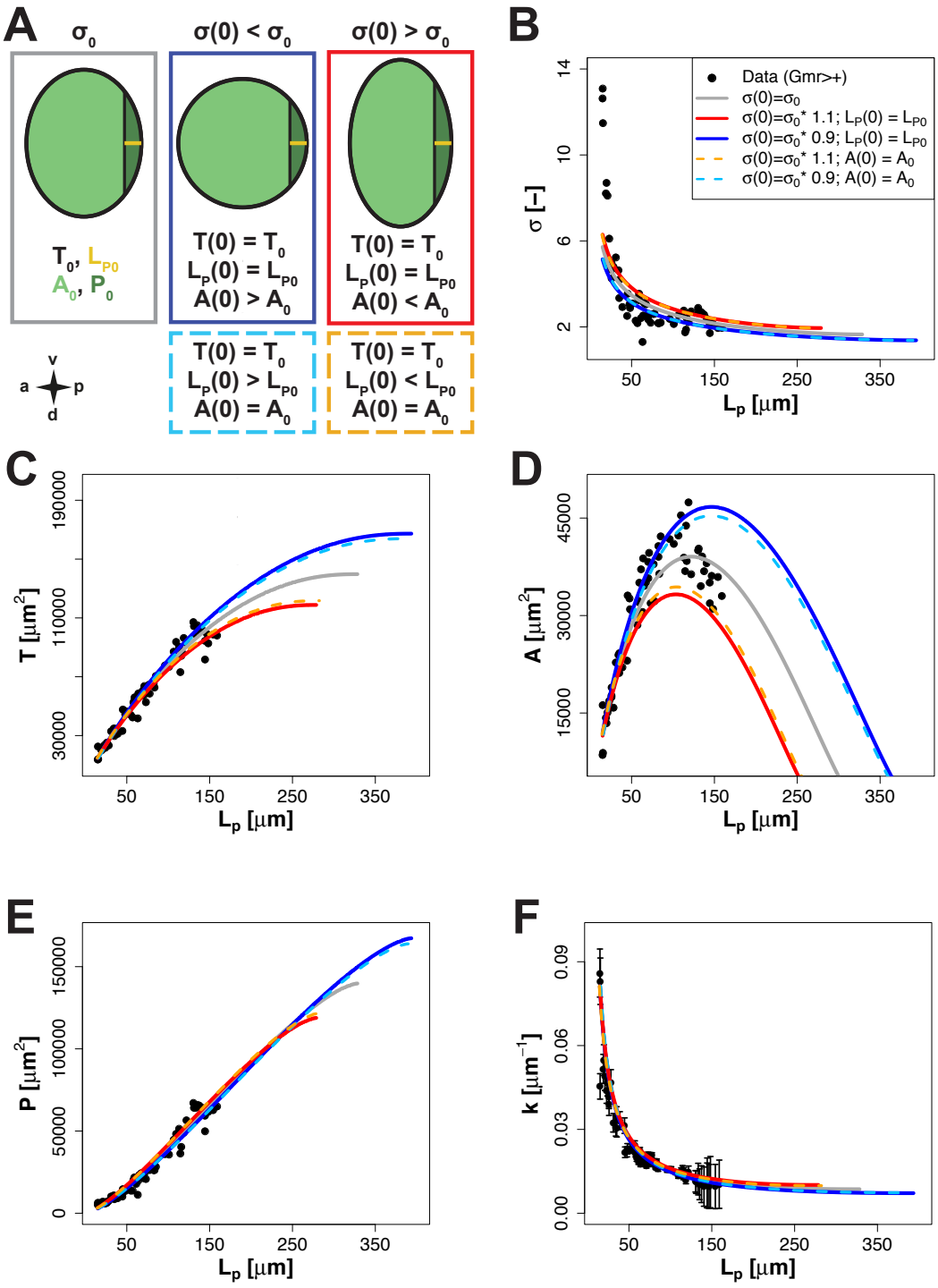

Figure S2: Impact of the initial shape on the growth kinetics and final size

To show the impact of the initial shape on the growth kinetics and the resulting final size, the initial shape was changed by 10% to a more elongated ($1.1 * \sigma_0$) or rounder ($0.9 * \sigma_0$) shape while keeping the initial total area T_0 constant. Here σ_0, L_{P0}, T_0, A_0 and P_0 refer to the initial shape, the initial posterior length and the initial total, anterior and posterior area obtained from fitting the *GMR>+* data set.

The area growth rate was assumed to follow the area-dependent decline (Eq. 2). The parameter values for the *GMR>+* data set were taken as the reference (supplementary table 1).

In a first case, the initial posterior length $L_P(0)$ and the initial total area T_0 were kept constant. As a consequence, the values for the initial anterior area A(0) and the posterior area P(0) were different (coloured solid lines) from the reference simulation (A_0, P_0, grey line). In a second case, the initial total area T_0 as well as the initial anterior (A(0)) and posterior (P(0)) areas were kept constant by modifying the initial posterior length $L_P(0)$ (coloured dashed lines), i.e. $A(0)= A_0$, $P(0)= P_0$ and $L_P(0)<L_{P0}$.

(A) Visualization of the different initial conditions chosen for the simulations.

(B-F) Growth kinetics for the different initial shapes and area distributions. Black dots: data for *GMR>+*; Grey line: reference simulation with parameters σ_0, T_0, A_0 obtained from fitting the *GMR>+* data set; Solid coloured lines: Varied shape, $L_p(0)$ as in the reference simulation; Dashed lines: Varied shape, area distribution as in the reference simulation.

A rounder initial shape (B-F, blue lines) leads to a bigger final total area independent of which measure ($L_p(0)$ or initial area distribution) is conserved.

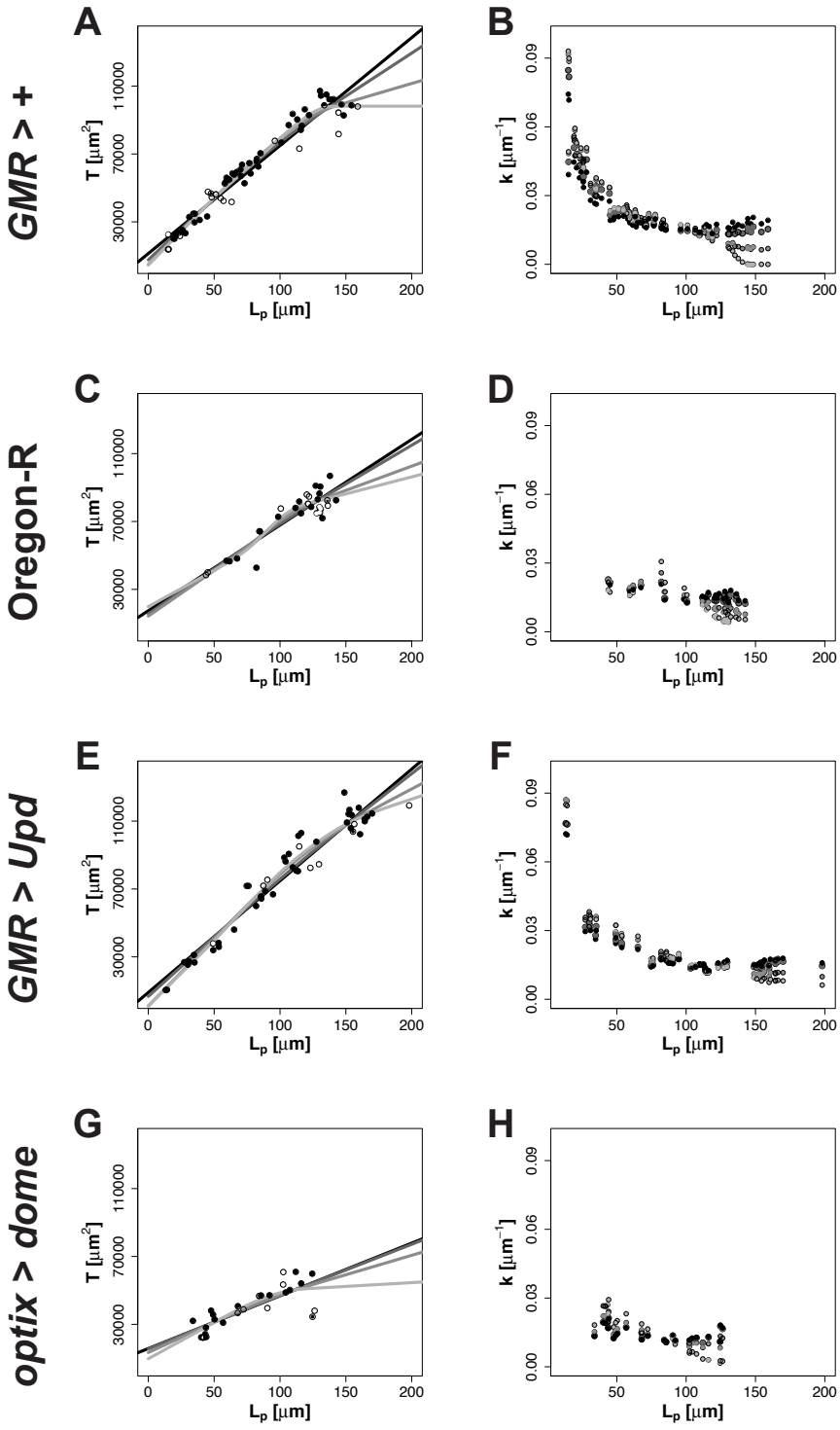

Figure S3: Estimation of area growth rates from the data

To estimate the area growth rates k from the data for the different genotypes, we used the same approach as described in (Vollmer et al., 2016) and Supplementary Text S2. The area growth rate *k* follows from

$$\frac{dT}{dL_P} = k(L_P) * A.$$

The area growth rate *k* can thus be obtained by dividing the slope in the total area T versus posterior length L_P plot by the respective anterior area A.

The genotypes are: (A,B) *GMR>+*; (C,D) Oregon-R; (E,F) *GMR>Upd*; (G,H) *optix>dome*;

(A,C,E,G) For each genotype, a linear model (black lines) as well as spline fits (grey lines) with varying degrees of freedoms were used to fit the increase of the total area T. Spline fits were used since the data might not be fitted perfectly using a linear model. The uncertainty in the estimate of the area growth rate *k* is thus highest where the models deviate most (see second column).

(B,D,F,H) The slope of the fits from the linear model and spline fits was divided by the anterior area A to obtain the area growth rate k. The colour code refers to the fits from the first column.

Data presented in panels (A)-(D) was taken from (Vollmer et al., 2016).

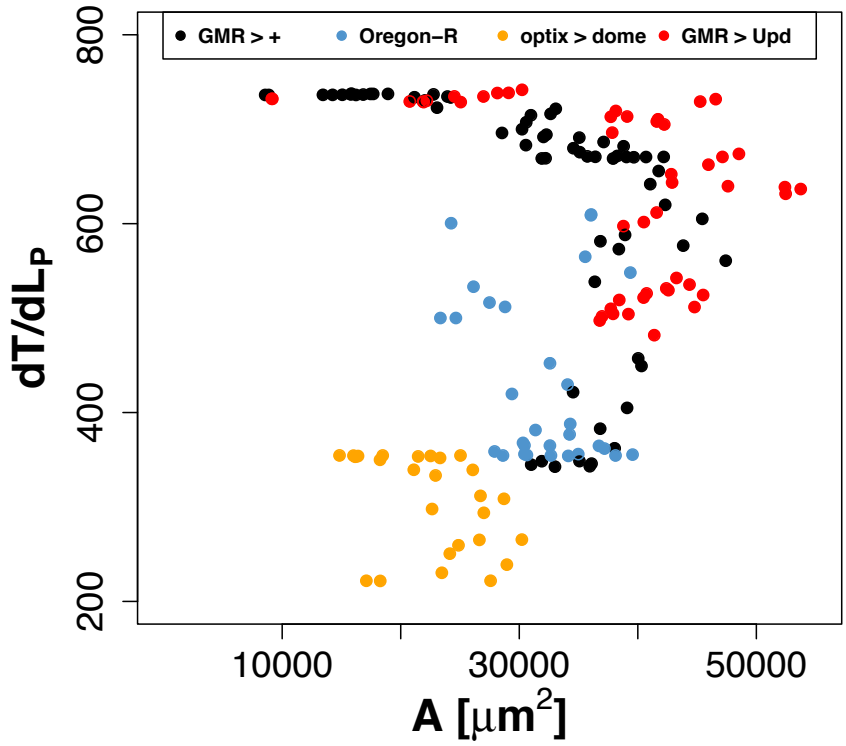

C

Figure S4: Growth kinetics in the different genotypes

Inferred average slope of the increase of the total area T with the posterior length L_p (Fig. S3) plotted versus the respective anterior area A for *GMR>+* (black), Oregon-R (blue), *optix>dome* (yellow) and *GMR>Upd* (red). The different genotypes fall into distinct regions in the plots, with some overlay of *GMR >+* and *GMR >UPD*.

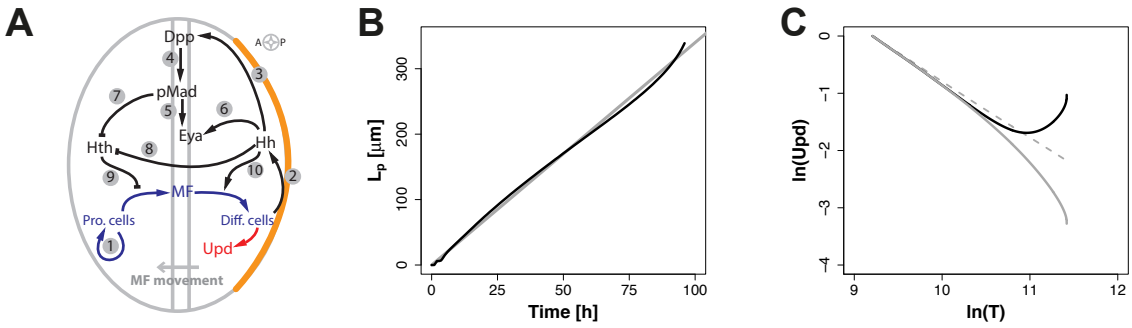

Figure S5: Impact of Upd production posterior to the MF on the Upd concentration in the eye disc

To model the impact of Upd production posterior to the MF, as is the case in the *GMR>Upd* genotype, we adapted a version of our model for eye disc patterning (Fried et al., 2016). All model parameters were kept as in the published version, but an Upd species was included that is produced by the differentiated cells Φ posterior to the MF (the domain of GMR-GAL4 expression). The initial concentration of Upd was set to 1 [a.u.]. Its concentration was assumed to be in steady state at the beginning of the simulation, i.e. when the MF starts to move. The growth rate was set to be directly proportional to the concentration of Upd. The initial (maximal) growth rate k_0 was set to the previously inferred value 0.0812 1/µm (Vollmer et al., 2016). As before (Fried et al., 2016), we modelled the growth of the eye disc using an incompressible Newtonian fluid. The Navier-Stokes equation is given as

$$\rho\left(\frac{\partial u}{\partial t} + (\nabla \cdot u)u\right) = -\nabla \mathrm{p} + \mu(\nabla^2 u + \frac{1}{3}\nabla(\nabla \cdot u))$$

$$\nabla \cdot u = S = \Pi \cdot k_0 \cdot c_{Upd}$$

with fluid density ρ, dynamic viscosity µ, and the local source or growth rate *S*. *u* denotes the fluid velocity field and c_{Upd} the concentration of *Upd*. Π denotes the area occupied by the proliferating cells, i.e. the area anterior to the MF. Additionally, Upd was set to be degraded everywhere in the disc with a half-life of 24 hours as inferred in this manuscript (Fig. 4), such that $\delta_{Upd} = \ln(2)/24$ [1/h]. Since the model was originally adapted to fit the speed measured by (Wartlick et al., 2014), the decay constant was adapted to the speed determined for Gmr>+ (Fig. 2A,B). The production rate was taken to be same as for the endogenous Upd that is produced before the start of the MF movement. As we use a Upd initial concentration of 1,

the endogenous production rate follows as $p_{Upd} = \delta_{Upd}$. The Upd diffusion coefficient was set to D_{Upd}=0.7 μm^2/s, as determined by FRAP in this manuscript (Fig. 3). In summary, we model the spatio-temporal evolution of all model components c_i using reaction-advection-dispersion equations according to

$$\frac{\partial c_i}{\partial t} + \nabla(\mathrm{u}c_i) = D_i \nabla^2 c_i + R_i.$$

The reaction term R_i for the Upd species in the GMR>Upd genotype reads

$$R_{Upd}^{Gmr>Upd} = \phi \cdot p_{Upd} - \delta \cdot c_{Upd}$$

, and for the Gmr>+ genotype,

$$R_{Upd}^{Gmr>+} = -\delta \cdot c_{Upd}.$$

(A) Complete model as published by (Fried et al., 2016) with the additional species Upd (marked in red).

(B) The MF moves about linearly with time in the model for the GMR>Upd genotype (black) and closely matches the position of an MF that advances at the previously measured speed of 3.4 μm/h (Vollmer et al., 2016; Wartlick et al., 2014).

(C) ln-ln plot of the Upd concentration at the center of the disc versus the total area T for three different genotypes. Black, solid line: A model of the GMR>Upd genotype. Upd is degraded, diluted and produced behind the MF. Grey, dashed line: Pure Dilution. A theoretical species that gets only diluted, but neither produced nor degraded. Grey, solid line: A model of the GMR>+ genotype. Upd gets diluted and degraded, but not produced. In all three cases, the concentration drops initially, mainly due to the growth and thus due to dilution, before production of Upd posterior to the MF can start and counteract the dilution and degradation. The biggest differences can only be observed towards the end of eye development. At this stage, pupation starts and no data could be obtained.

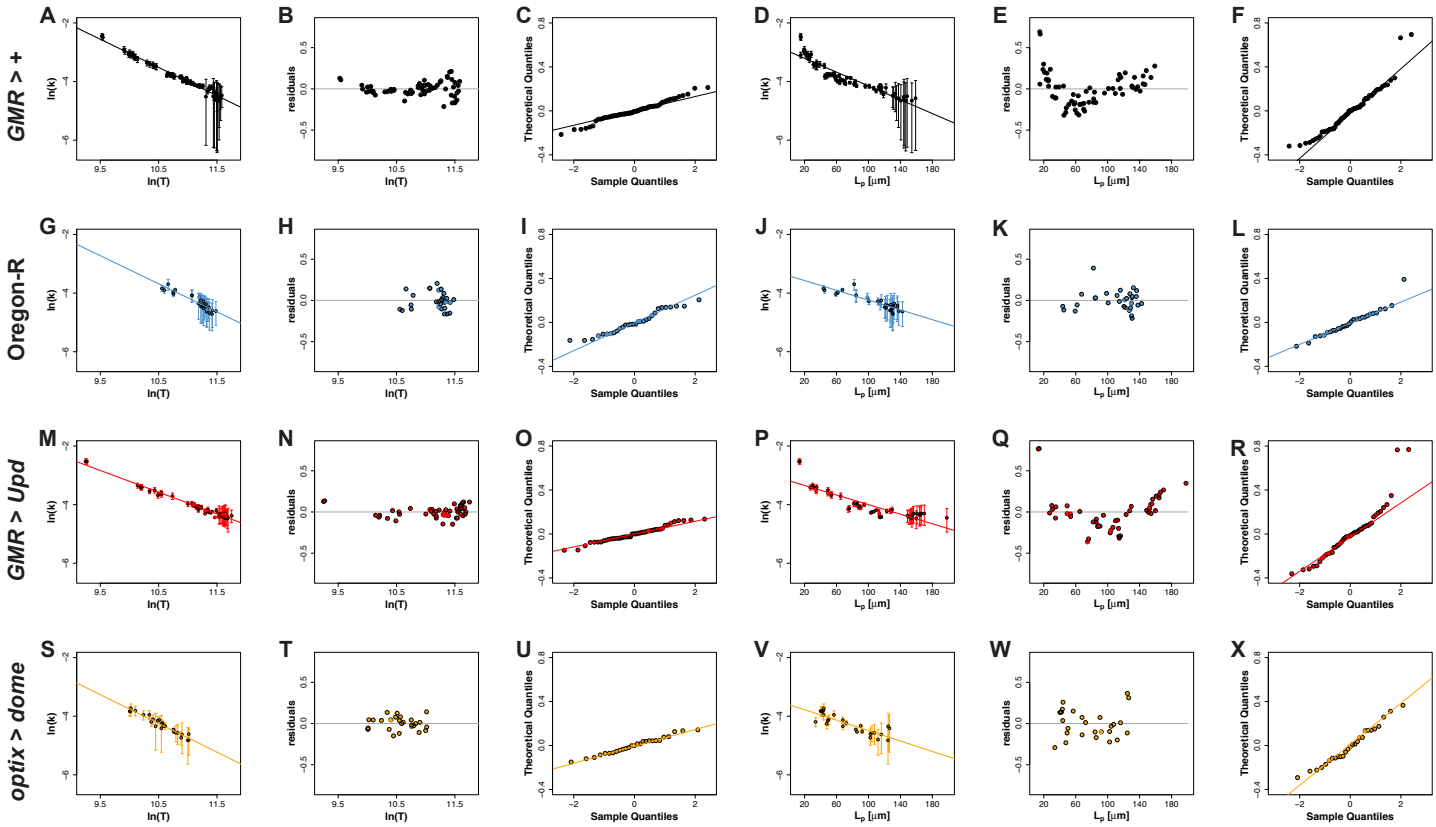

Figure S6: Residuals and analysis of the normality of the linear fits to the area growth rate *k*

Fit, residuals and QQ-plot for ln(k) versus ln(T) and ln(k) versus L_P for the data sets of the different genotypes.

(A-F) *GMR>+*; (G-L) Oregon-R; (M-R) *GMR>Upd*; (S-X) *optix>dome*

A systematic trend with the highest positive deviations of the residuals at small and big posterior lengths L_P and negative deviations at intermediate posterior lengths can be seen for the *GMR>+* and *GMR>Upd* data set when fitting a linear model to ln(k) versus L_P (panels E and K).

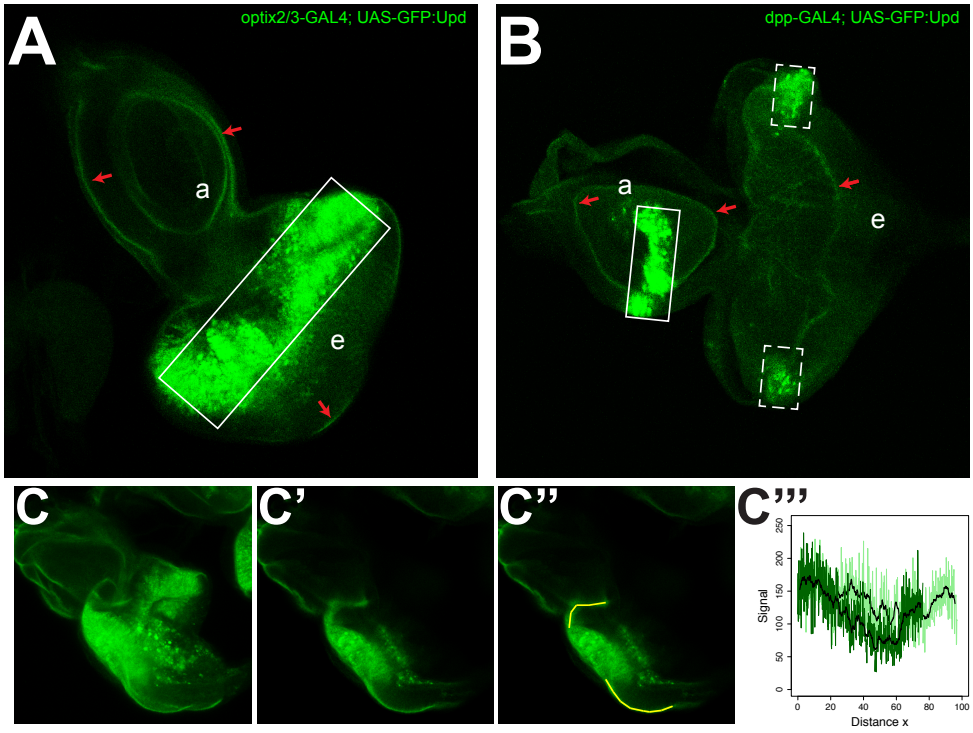

Figure S7: Expression of GFP:Upd in different domains of the eye–antennal disc results in uniform and widespread dispersion of GFP:Upd.

Eye-antennal imaginal discs expressing GFP:Upd under the control of different GAL4 drivers (A,B). The expression domains are marked by white boxes. (A) *optix2/3-GAL4; UAS-GFP:Upd*. GFP:Upd is expressed in a central region of the eye disc; (B) *dpp^{blk}-GAL4; UAS-GFP:Upd*. GFP:Upd is produced in an antennal domain (boxed, solid line) and in two weaker lateral eye domains (boxed, dashed line). In both genotypes, and in addition to the production domains, GFP:Upd is detected with uniform intensity on the apical surface of the epithelium. Red arrows point to some of these epithelial surfaces. "a" antennal disc region; "e" eye disc region. Anterior is left and dorsal is up in (A,B). The *optix2/3-GAL4* and *dpp^{blk}-GAL4* driver lines are described in (Neto et al., 2016; Ostrin et al., 2006) and (Staehling-Hampton et al., 1994), respectively. (C-C''') Lateral view of an eye imaginal disc where GFP:Upd is expressed under the control of optix2/3. (C) Maximum intensity projection; (C') Single image plane; (C'' and C'''') Quantification of the intensity profile along the marked lines (yellow, C'') into posterior direction (light green) and anterior direction (dark green). Raw profiles (coloured) and moving average (black) are shown. The intensity profiles overlap arguing against a directed movement of GFP:Upd.

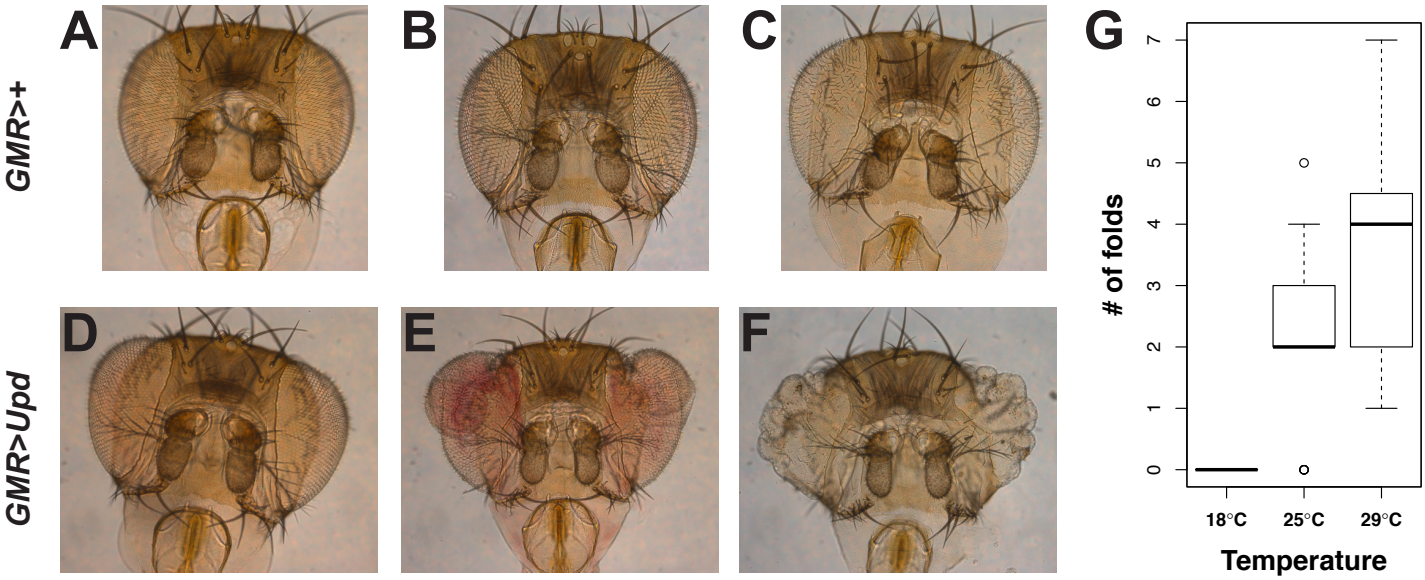

Figure S8: The eye overgrowth phenotype is temperature sensitive between 18°C and 29°C

Control (*Gmr>+*) and flies with *upd* expression driven by the *GMR*-GAL4 line in differentiated cells (*GMR>Upd*) were raised at 18°C (A, D), 25°C (B,E), and 29°C (C,F). While there are no big changes of eye sizes in adult flies for the control strain (A-C), there is a clear increase in the eye overgrowth with higher temperatures in the *GMR>Upd* genotype (D-F). This indicates that signalling downstream of Upd is not saturated at the intermediate temperature of 25°C, at which the experiments for the determination of the molecular properties of Upd were carried out. Due to the massive overgrowth, folding of the adult eye occurs in the *GMR>Upd* genotype (D-F). Thus, eye area as previously measured in 2 dimensions on flat images (Fig. 1A), is not an appropriate measure anymore, as it cannot account for the increased area due to the folding. Therefore, numbers of folds were used as a measure of overgrowth for the *GMR>Upd* genotype instead (H). Visual inspection (D-F) and numbers of folds (H) confirm the sensitivity of the system at increasing temperatures. Number of flies analysed for panel H: 18°C, n=11; 25°C, n=12; 29°C, n=9; Panels A-F are representative sample images from the flies analysed.

REFERENCES

Abràmoff, M. D., Magalhães, P. J. and Ram, S. J. (2004). Image processing with ImageJ. *Biophotonics Int.* **11**, 36–42.

Bach, E. a, Vincent, S., Zeidler, M. P. and Perrimon, N. (2003). A sensitized genetic screen to identify novel regulators and components of the Drosophila janus kinase/signal transducer and activator of transcription pathway. *Genetics* **165**, 1149–66.

Coleman, T. F. and Li, Y. (1996). An Interior Trust Region Approach for Nonlinear Minimization Subject to Bounds. *SIAM J. Optim.* **6**, 418–445.

Fried, P., Sánchez-Aragón, M., Aguilar-Hidalgo, D., Lehtinen, B., Casares, F. and Iber, D. (2016). A Model of the Spatio-temporal Dynamics of Drosophila Eye Disc Development. *PLoS Comput. Biol.* **12**, e1005052.

Garcia-Bellido, A. (1965). Larvalentwicklung transplantierter Organe von Drosophila melanogaster im Adultmilieu. *J. Insect Physiol.* **11**, 1071–1078.

Kang, M., Day, C. A., Kenworthy, A. K. and DiBenedetto, E. (2012). Simplified equation to extract diffusion coefficients from confocal FRAP data. *Traffic* **13**, 1589–600.

Kicheva, A., Pantazis, P., Bollenbach, T., Kalaidzidis, Y., Bittig, T., Jülicher, F. and González-Gaitán, M. (2007). Kinetics of morphogen gradient formation. *Science* **315**, 521–5.

Neto, M., Aguilar-Hidalgo, D. and Casares, F. (2016). Increased avidity for Dpp/BMP2 maintains the proliferation of progenitors-like cells in the Drosophila eye. *Dev. Biol.* **418**, 98–107.

Ostrin, E. J., Li, Y., Hoffman, K., Liu, J., Wang, K., Zhang, L., Mardon, G. and Chen, R. (2006). Genome-wide identification of direct targets of the Drosophila retinal determination protein Eyeless. *Genome Res.* **16**, 466–476.

Staehling-Hampton, K., Jackson, P. D., Clark, M. J., Brand, A. H. and Hoffmann, F. M. (1994). Specificity of bone morphogenetic protein-related factors: Cell fate and gene expression changes in Drosophila embryos induced by decapentaplegic but not 60A. *Cell Growth Differ.* **5**, 585–593.

Tsai, Y.-C. and Sun, Y. H. (2004). Long-range effect of upd, a ligand for Jak/STAT pathway, on cell cycle in Drosophila eye development. *Genesis* **39**, 141–53.

Vollmer, J., Fried, P., Sánchez-Aragón, M., Lopes, C. S., Casares, F. and Iber, D. (2016). A quantitative analysis of growth control in the Drosophila eye disc. *Development* **143**, 1482–90.

Wartlick, O., Jülicher, F. and Gonzalez-Gaitan, M. (2014). Growth control by a moving morphogen gradient during Drosophila eye development. *Development* **141**, 1884–93.